Chinese Chemical Letters 36 (2025) 110381

Contents lists available at ScienceDirect

Chinese Chemical Letters

journal homepage: www.elsevier.com/locate/cclet

Tailor-made overstable 3D carbon superstructures towards efficient zinc-ion storage

Chengmin Hu[a], Pingxuan Liu[a], Ziyang Song[a], Yaokang Lv[b], Hui Duan[a], Li Xie[c,d], Ling Miao[a,*], Mingxian Liu[a,*], Lihua Gan[a,*]

[a] Shanghai Key Lab of Chemical Assessment and Sustainability, School of Chemical Science and Engineering, Tongji University, Shanghai 200092, China
[b] College of Chemical Engineering, Zhejiang University of Technology, Hangzhou 310014, China
[c] Key Laboratory of Yangtze River Water Environment Ministry of Education, College of Environmental Science and Engineering, Tongji University, Shanghai 200092, China
[d] Shanghai Institute of Pollution Control and Ecological Security, Shanghai 200092, China

ARTICLE INFO

Article history:
Received 27 June 2024
Revised 23 July 2024
Accepted 28 August 2024
Available online 30 August 2024

Keywords:
Tailor-made
Overstable
Carbon superstructures
High serformance
Zinc-ion storage

ABSTRACT

Designing carbon materials with ideal stable hierarchical porous structures and flexible functional properties for efficient and sustainable Zn^{2+} ion storage still faces great challenges. Herein, the three-dimensional carbon superstructures with spherical nanoflower-like structures were tailor-made by the self-assembly strategy. Specifically, organic polymer units (*i.e.*, organic motifs) were formed by tetrachloro-*p*-benzoquinone (TBQ) and 2,6-diamino anthraquinone (DAQ) *via* a noble-metal-free catalyzed coupling reaction. Subsequently, the organic motifs assemble into spherical nanoflower-like superstructures induced by intermolecular hydrogen bonding and aromatic π-π stacking interactions. Well-designed carbon superstructures can provide a stable backbone that effectively blocks structural stacking and collapse. Meanwhile, the hierarchical porous structures in 3D carbon superstructures provide continuous charge transport pathways to greatly shorten the ion diffusion distance, and as a result, the carbon superstructures-based zinc-ion hybrid capacitors (ZIHCs) provide a capacity of 245 mAh/g at 0.5 A/g, a high energy density of 152 Wh/kg and an ultra-long life of 300,000 cycles at 20 A/g. The excellent electrochemical performance is also attributed to the corresponding charge storage mechanism, *i.e.*, the alternate binding of $Zn^{2+}/CF_3SO_3^-$ ions. Besides, the high-level N/O motifs improve the surface properties of the carbon superstructures and reduce the ion migration barriers for more efficient charge storage. This paper provides insights into the design of advanced carbon-based cathodes and presents a fundamental understanding of their charge storage mechanisms.

With increasing energy demand and serious environmental pollution, environmentally safe aqueous energy storage devices have attracted the attention of researchers. Among them, zinc-ion hybrid capacitors (ZIHCs), as an emerging energy storage device, are considered one of the most promising candidates for energy storage systems because of their excellent performance, rich reserves and high safety [1–3]. ZIHCs consist of a battery-type anode and a capacitor-type cathode coupled in an aqueous electrolyte [4–10]. It combines the advantages of batteries and capacitors to enhance the power output and cycle life of the device while ensuring that the energy density of the device is not compromised [11–14]. However, for ZIHCs, the reaction kinetic imbalance between the two electrodes is the main problem faced due to the different energy storage mechanisms of the anode and cathode [15–17]. Specifically, *i.e.*, battery-type anodes provide high capacity through zinc-ion deposition/stripping reactions, while capacitor-type electrodes provide excellent power output through fast ion adsorption/desorption process [18–20]. To achieve the matching of capacity and power output, a lot of research has been carried out in recent years to develop the electrochemical performance of cathode materials.

Until now, various carbon materials have been reported to be used as cathode materials for ZIHCs [21–23]. One-dimensional carbon-based materials, such as carbon nanotubes and carbon fibers, have high surface areas and large aspect ratios [24,25]. However, the narrow pore size distribution reduces ion accessi-

* Corresponding authors.
E-mail addresses: 22169@tongji.edu.cn (L. Miao), liumx@tongji.edu.cn (M. Liu), ganlh@tongji.edu.cn (L. Gan).

https://doi.org/10.1016/j.cclet.2024.110381
1001-8417/

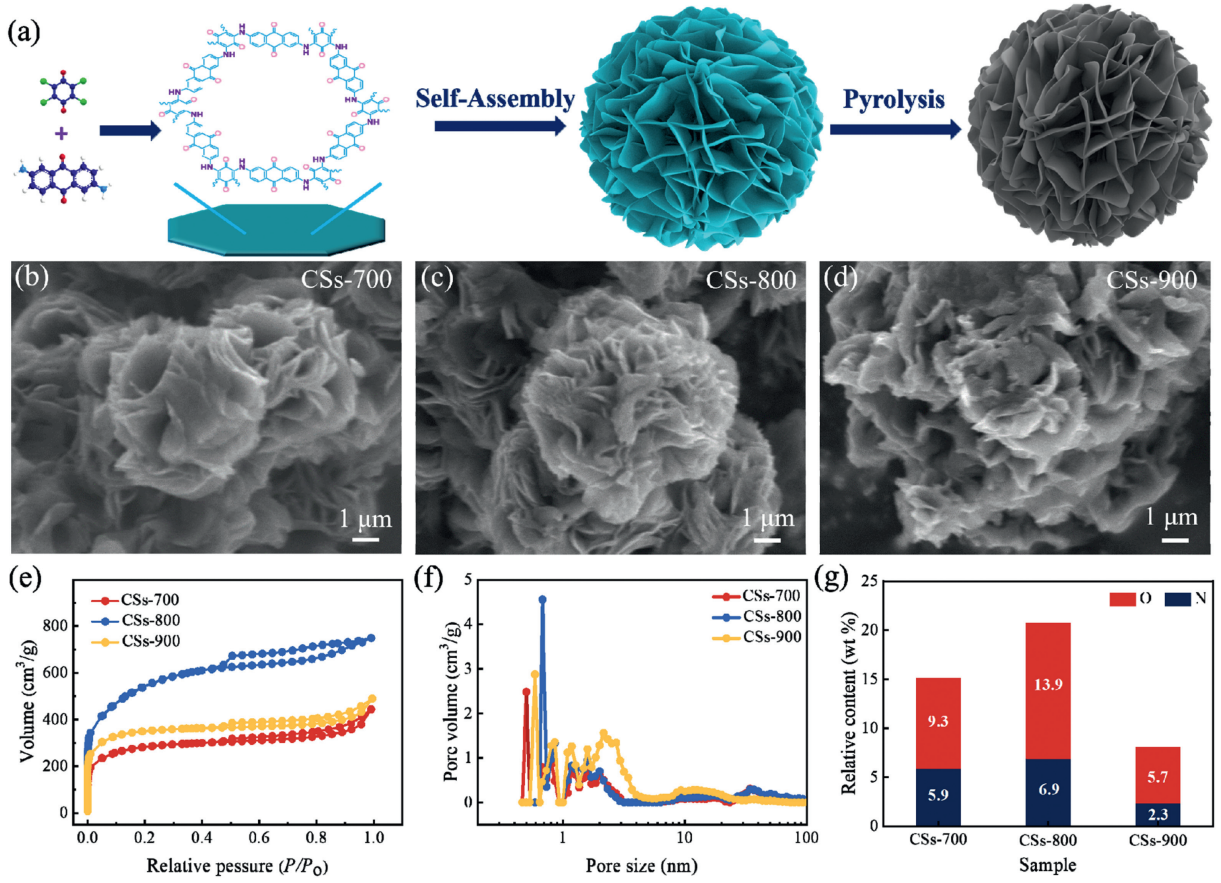

Fig. 1. (a) Formation process of carbon superstructures. (b-d) SEM images of CSs-X. (e) Nitrogen absorption-desorption isotherms and (f) corresponding pore size distribution curves. (g) Heteroatom contents.

bility. Two-dimensional carbon-based materials, such as graphene and layered porous carbon, have structured monolayer carbon networks [25–28]. However, interactions between carbon nanosheets make them prone to restacking, leading to nanopore instability [29,30]. The low ionic accessibility and limited pore utilization of low-dimensional carbon materials greatly hinder the efficient storage of zinc ions, leading to low zincophilic activity and slow reaction kinetics. Three-dimensional carbon frameworks with high specific surface area, reasonably hierarchical porosity and large conductive networks are considered promising ZIHCs cathodes [31–33]. The superior three-dimensional carbon structures (*e.g.*, pencil shaving derived porous carbon [34], MOF-derived porous carbon [35]) are helpful in enhancing the transport effect of ions and producing fast reaction kinetics [36,37]. In addition, the introduced heteroatoms also help to improve the surface properties of the carbon cathode and provide an additional platform for zinc-ion storage [38–42]. Therefore, the three-dimensional cathode structure must be accurately designed to match the zinc anode to achieve efficient zinc-ion storage.

Here, a three-dimensional spherical nanoflower carbon superstructure was constructed by the self-assembly strategy. First, tetrachloro-*p*-benzoquinone (TBQ) and 2,6-diaminoanthraquinone (DAQ) formed into organic motifs by a noble metal-free catalyzed coupling reaction and then the organic motifs assembled into superstructures by hydrogen bonding and π-π stacking interactions. The well-designed carbon superstructures have robust frameworks and multi-scale continuous charge transport channels, ensuring excellent stability and fast reaction kinetics. Ultra-high N/O doping improves interfacial wettability, while Faraday properties provide additional capacity. As expected, carbon superstructures-based ZIHCs can provide high energy densities (152 Wh/kg) and ultra-long lifespans (300,000 cycles). The excellent electrochemical performance is attributed to the well-designed carbon superstructures and the appropriate charge storage mechanism, *i.e.*, the alternate binding of Zn^{2+}/$CF_3SO_3^-$ ions in the carbon active sites. This work provides new insights into the design of advanced carbon-based cathodes and fundamentally elucidates the charge storage mechanisms.

The synthesis of carbon superstructures is divided into three steps. The first step is to synthesize the organic motifs by coupling reaction of tetrachloro-*p*-benzoquinone (TBQ) and 2,6-diaminoanthraquinone (DAQ). The second step is the self-assembly of organic motifs *via* hydrogen bonding and π-π stacking interactions to form spherical nanoflower-like superstructures. The third step is pyrolysis, where the nanoflower-like superstructures are pyrolyzed to form well-designed carbon superstructures (Fig. 1a). The tailored carbon superstructures are named CSs-X, where X represents the carbonization temperature of 700, 800 and 900 °C (see the detailed experimental section in Supporting information). The disappearance of the infrared absorption characteristic peaks at 750 cm^{-1} for C–Cl and 1130 cm^{-1} for $-NH_2$ groups in the monomer and the appearance of the characteristic peak at 1530 cm^{-1} for –NH– group belonging to the organic motifs in FTIR spectra indicate the coupling reaction of TBQ with DAQ was successful (Fig. S1a in Supporting information). Carbon superstructures prepared by pyrolysis at different temperatures. The inherent conjugated structure of the organic motifs results in a nanoscale flower morphology stacked layer-by-layer (Fig. S1b in Supporting information). After pyrolysis at 700 °C, the CSs-700 shows aggregated stacked morphology features suggesting incomplete car-

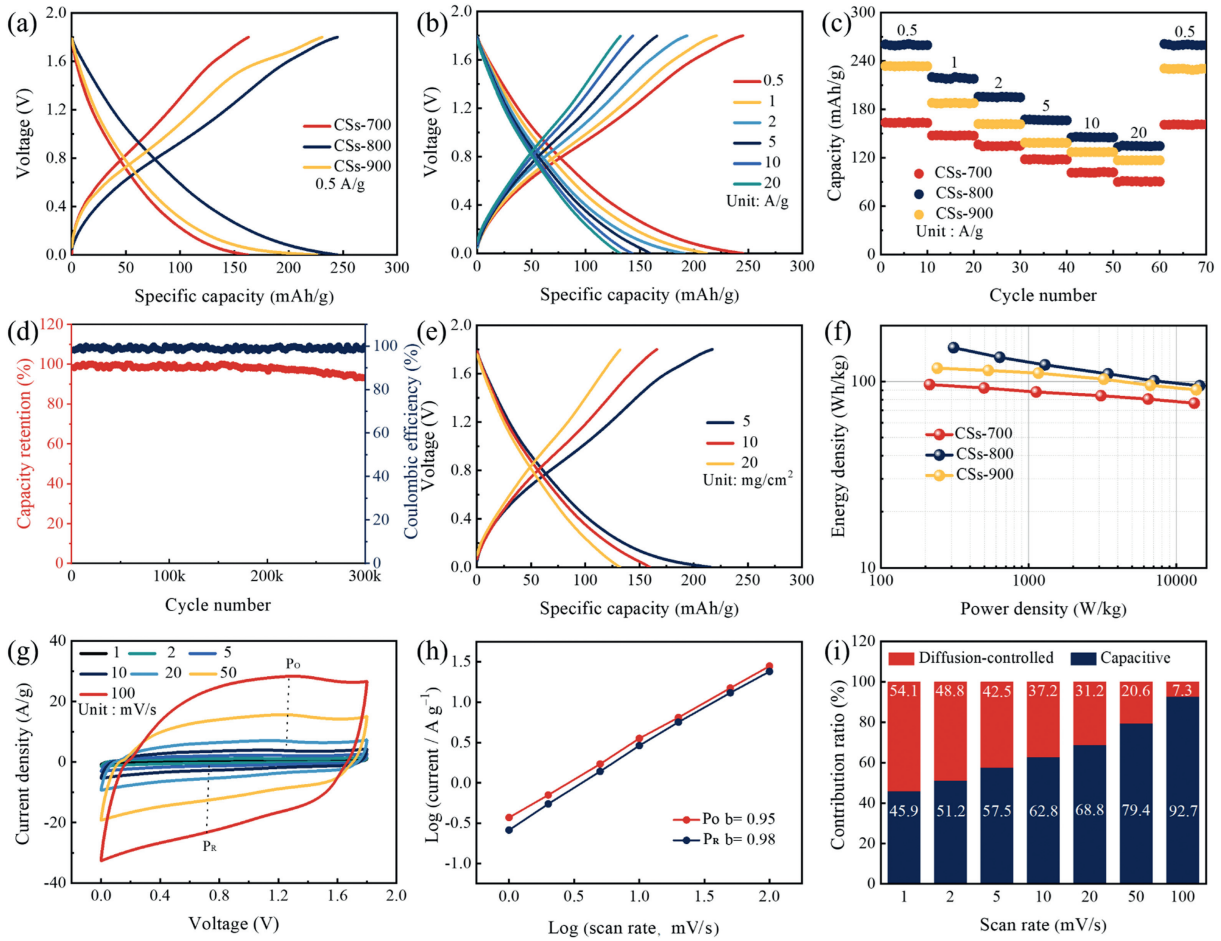

Fig. 2. Electrochemical evaluation of the CSs-based ZIHCs. (a) Voltage–capacity profiles. (b) GCD curves of CSs-800 based ZIHCs at various current densities. (c) Rate performance. (d) Specific capacities of CSs-800 based ZIHCs under different mass loadings. (e) Ragone plots. (f) Cyclability of CSs-800 based ZIHCs. (g) CV curves of CSs-800. (h) Calculation *b* value. (i) Normalized capacitive and diffusion-controlled contribution ratios at various scan rates of CSs-800 based ZIHCs.

bonization of the carbon superstructure (Fig. 1b), while the CSs-900 occurs a certain collapse when the temperature reaches 900 °C (Fig. 1d). The CSs obtained at 800 °C (CSs-800) perfectly preserve the nanoflower structure of the precursor, which is the most suitable pyrolysis temperature (Fig. 1c).

N_2 adsorption/desorption tests provide more detailed data analysis of pore size parameters in CSs-X. N_2 adsorption/desorption curves of CSs-X show a hierarchical porous structure (Fig. 1e). The specific surface areas of CSs-700, 800, and 900 are 1097, 1789, and 901 m^2/g, respectively. CSs-800 inherit the good structural design of the organic superstructure, thus showing the highest specific surface area and optimal pore size distribution. Specifically, the mesopore volumes of CSs-700, 800, and 900 are 0.65, 1.12, and 0.57 cm^3/g. CSs-800 possesses the largest average pore size of 2.49 nm, whereas CSs-700 and CSs-900 have average pore sizes of 2.45 and 2.26 nm, respectively (Table S1 in Supporting information). As shown in Fig. 1f, the micropore size distribution of CSs-X is concentrated between 0.5 nm and 1.3 nm. The differences in pore structure of CSs-X are attributed to the variations in the degree of carbonization. Too high or too low pyrolysis temperatures can lead to structural instability, resulting in low SSA and unreasonable pore size distribution. The stable structure of CSs-800 promotes rapid penetration of electrolyte ions, and the reasonable pore size distribution provides sufficient storage platform, resulting in enhanced capacity and energy density.

X-ray photoelectron spectroscopy (XPS) was used to analyze the amount of heteroatoms and the chemical condition of N/O atoms in the carbon superstructures [43,44]. Three characteristic peaks are monitored in the XPS spectra, as C 1s (284.4 eV), N 1s (399 eV), and O 1s (520 eV), respectively (Fig. S2a in Supporting information) [45,46]. Specifically, the N doping of CSs-X are 5.9, 6.9 and 2.3 wt%, and the O doping are 9.3, 13.9 and 5.7 wt%, corresponding to CSs-700, CSs-800 and CSs-900, respectively (Fig. 1g). CSs-800 has the highest heteroatom doping, which is attributed to the favorable properties due to the appropriate pyrolysis temperature. High-resolution spectra of N 1s show three signal peaks located at 398.2 eV, 400 eV and 401.3 eV corresponding to pyridine-N (N-6), pyrrole-N (N-5), and quaternary ammonium-N (N-Q), respectively (Fig. S2b in Supporting information). Among them, pyridine-N with electrochemically active occupies the largest percentage, which allows them to provide storage sites for Zn^{2+} storage, resulting in additional capacity. High-resolution spectra of O 1s peaks show three distinct signal peaks at 531.3 eV (C=O), 532.7 eV (C–OH/C–O–C) and 533.9 eV (-COOH), respectively. Substantial heteroatom doping can greatly improve the surface wettability of CSs-X and provide additional pseudocapacitance [47–49]. Next, X-ray diffraction (XRD) tests were carried out to investigate the crystal structure of the CSs-X. As shown in Fig. S3a (Supporting information), CSs-X show two small bulges at 24.6° and 44.1° attributed to the 002 and 100 crystal planes of the carbon lattice, respectively [18,50]. Wide and weak bulges indicate the presence of amorphous organization in the CSs-X, which can provide an abundant active platform for storing zinc ions. Raman spectra of CSs-X show two broad peaks at 1350 cm^{-1} for the D band caused by defects/doping in the carbon

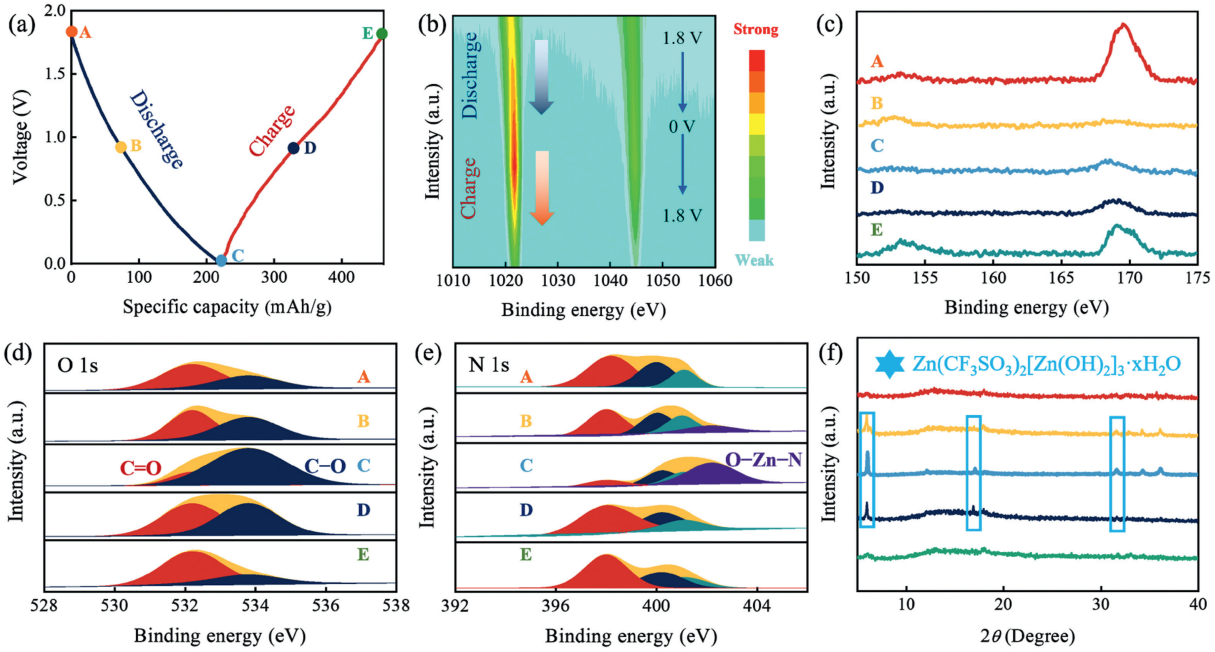

Fig. 3. (a) A GCD profile. (b) *Ex-situ* XRD patterns. *Ex-situ* XPS spectra of (c) Zn 2p, (d) S 2p/2s, (e) N 1s and (f) O 1s at various discharged/charged states.

lattice and G band at 1550 cm^{-1} for the sp^2 benzene ring carbon (Fig. S3b in Supporting information) [51–53]. The degree of defects and doping in the CSs-X can be calculated from the peak area ratio of I_D/I_G. Remarkably, the I_D/I_G values of CSs-700, 800, and 900 are 1.8, 2.1, and 1.6, respectively. CSs-800 has the largest I_D/I_G value, indicating that it has the most abundant storage active sites.

ZIHCs were assembled in an aqueous electrolyte of 3 mol/L $Zn(CF_3SO_3)_2$ with CSs-X as the working cathode and zinc foil as the anode. As shown in Fig. 2a, CSs-700, 800 and 900 deliver 162, 245, and 225 mAh/g at 0.5 A/g, respectively. The capacity of the conductive agent (super P) shows a neglected contribution (Fig. S4 in Supporting information). When the current density increases to 20 A/g, CSs-800 still delivers 130 mAh/g (Fig. 2b), which is also far better than CSs-700 (91 mAh/g) and CSs-900 (104 mAh/g), demonstrating its superior capacity retention (Fig. S5 in Supporting information). Additionally, the CSs-X based ZIHCs show highly reversible capacity at all current densities (Fig. 2c). When using 2 mol/L $ZnSO_4$ as the electrolyte, CSs-800 still has favorable electrochemical performance (Fig. S6 in Supporting information). Remarkably, CSs-800 maintains 92.7% capacity after 300,000 cycles at 10 A/g (Fig. 2d), while the CSs-700 and CSs-900 are 87.7% and 89.1%, respectively (Fig. S7 in Supporting information). CV curves also did not change significantly after long cycles, reaffirming the stability of the CSs-800 cathode (Fig. S8 in Supporting information). High mass-loading performance remains an important guideline for realizing large-scale applications [54], with CSs-800 can deliver capacities of 260, 160, and 132 mAh/g when mass-loading isotropy increases to 5, 10, and 20 mg/cm^2 (Fig. 2e). Based on the mass of cathode active materials, such a high capacity of CSs-800 provides a high energy density of 152 Wh/kg at a power density of 309 W/kg. The electrochemical performance of CSs-800 is quite encouraging compared to CSs-700, 900 and recently reported carbon-based ZIHCs (Fig. 2f and Table S2 in Supporting information).

The ion diffusion behavior and reaction kinetics of CSs-based ZIHCs were investigated by electrochemical impedance spectroscopy (EIS), which was used to reveal the potential reasons for the excellent electrochemical performance (Fig. S9 in Supporting information). Nyquist plots show that CSs-800 based ZIHCs have the smallest interfacial resistances (R_s) of 0.8 Ω, while CSs-700 and CSs-900 are 1.5, and 1.2 Ω, respectively. The charge transfer resistances (R_{ct}) for CSs-700, CSs-800, and CSs-900 are 18, 12 and 22 Ω, respectively (Table S3 in Supporting information). CSs-800 has the smallest R_s and R_{ct}, which is attributed to the good modification of the carbon superstructure interface by the highly active N/O doping, which improves the electrode surface compatibility and lowers the charge transfer barrier (Fig. S10 in Supporting information) [55–57]. CV profiles at scan rates from 1 mV/s to 100 mV/s show one pair of redox peaks (marked P_O/P_R, Fig. 2g). Dunn's method [58–60] shows that the connection between current and scan rate is $i = kv^b$, where k is a constant. The logarithmic relationship between v and i, b, is used to explain the capacitance diffusion. The b value approaches 1, which represents a perfect surface control process [61–64]. At the range of 10–100 mV/s, the b value of CSs-800 is 0.95/0.98 (Fig. 2h), while the b values of CSs-700 and CSs-900 are 0.88/0.92 and 0.86/0.82, respectively (Fig. S11 in Supporting information). The b value of CSs-800 is close to 1, which indicates that the rapid ion diffusion process, corresponds to the fast reaction kinetics.

The specific calculations of the contributions of capacitance control and diffusion control to the storage process are further carried out using following Eqs. 1 and 2:

$$i = k_1 v + k_2 v^{0.5} \quad (1)$$

$$i/v^{0.5} = k_1 v^{0.5} + k_2 \quad (2)$$

where k_1 and k_2 are constants, $k_1 v$ and $k_2 v^{0.5}$ are used as representatives of the capacitance-controlled and diffusion-controlled contributions to the storage process, respectively [65–67]. According to the equation, the capacitance contribution of CSs-800 cathode at 1 mV/s is 45.9% (Fig. 2i). The capacitance contribution of the CSs-800 cathode increases from 51.2% to 92.7% as scan rate increases from 2 mV/s to 100 mV/s. The capacitive contribution of CSs-700 and CSs-900 is 85.1% and 90.0%, respectively (Fig. S12 in Supporting information). CSs-800 shows typical capacitance control mechanisms, which are attributed to theinterconnected network to provide fast ion transport and the highest N/O doping lowering the

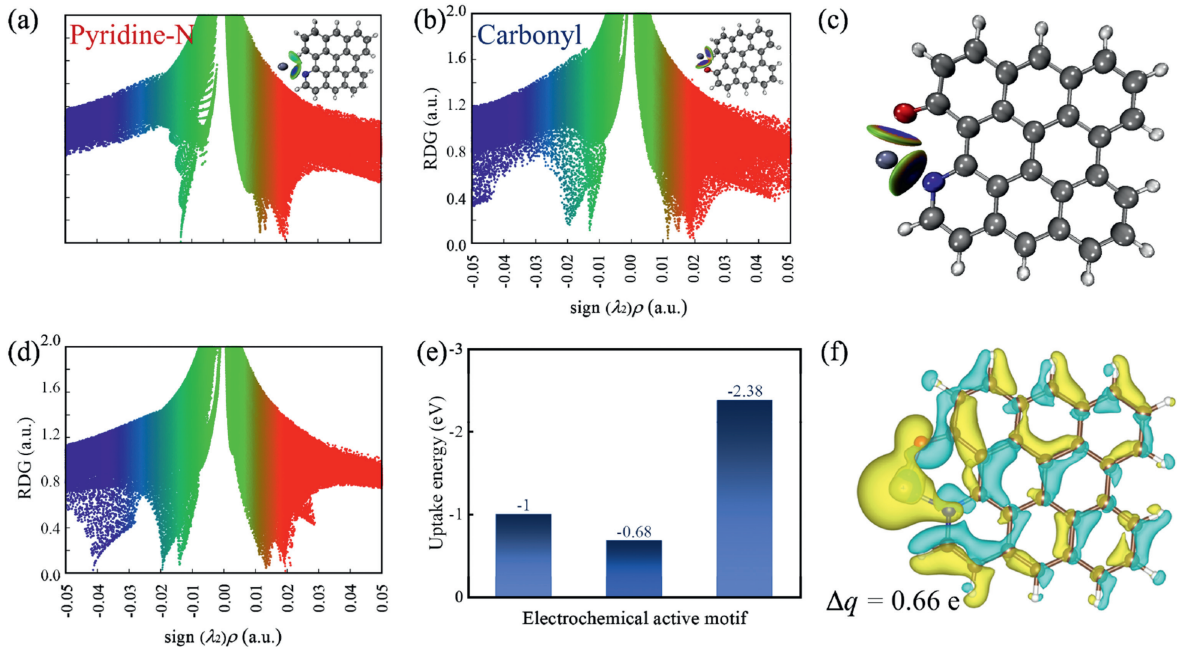

Fig. 4. Plots of RDG *versus* sign(λ_2)ρ for (a) pyridine-N, (b) carbonyl O. (c) Synergetic carbonylic/pyridine-N model. (d) Corresponding RDG plot. (e) The uptake energy values and (f) differential electron density isosurface of single Zn^{2+} adsorbed on the optimized redox-active synergetic carbonylic/pyridine sites.

adsorption and desorption energy barriers to produce fast charging and discharging kinetics.

Five electrode sheet states were selected for monitoring at different voltages during a single charge/discharge cycle, labeled sequentially as A, B, C, D, and E. Of these, A, B, and C are the three state points of discharge to 1.8 V, 0.9 V, and 0 V, and D and E are the two state points of charge to 0.9 V and 1.8 V (Fig. 3a). To gain insight into the charge storage mechanism, a series of *ex-situ* characterizations were carried out to observe and analyze the changes in electrode structure and morphology. *Ex-situ* XPS spectra were performed to monitor the valence changes of the elements (Fig. S13 in Supporting information). Expanding, when the cathode sheet undergoes discharge from state A to C (1.8 V to 0 V), Zn^{2+} ions are stripped from the Zn foil and gradually aggregate and adsorb on the CSs-800 cathode. As a result, Zn 2p signals gradually elevate during this discharge process. When the cathode sheet is charged from state C to E (0–1.8 V), the Zn 2p signals gradually weaken again (Fig. 3b). Meanwhile, S 2p/2s, which represents the $CF_3SO_3^-$ signal, shows an opposite trend to Zn 2p signals (Fig. 3c). This suggests that simultaneous anion and cation storage occurs during a single electrochemical storage process. Specifically, the storage of Zn^{2+} ions during the discharge process and the coupling of $CF_3SO_3^-$ ions during the charging process. The reversible transformation of Zn 2p and S 2p/2s signals is attributed to the fast ionic response and structural storage stability guided by the tailored carbon superstructure.

Volume-integrated fitting of *ex-situ* high-resolution O 1s and N 1s spectra to reveal the effect of N/O atoms in the alternating cation/anion storage process. When discharge from 1.8 V to 0 V (states A to C), the content of C=O located at 532.2 eV decreases significantly, while the content of C−O located at 533.8 eV increases significantly. Upon recharging to 1.8 V (states C to E), the C=O/C−O content returns to the initial state (Fig. 3d). This indicates the reversible storage of electrically active C=O with Zn^{2+} ions. For N species, *ex-situ* high-resolution N 1s show threesignal peaks, pyridine-N at 399 eV, pyrrole-N at 400.2 eV, and quaternary-N at 401.1 eV (Fig. 3e). Pyridine-N with electrochemically active shows a reversible trend of enhancement followed by weakening and then enhancement in a single charge/discharge cycle. The signal peak attributed to the O−Zn−N bond is monitored at 402.2 eV [68], which indicates that the co-modification of pyridine-N and C=O groups can greatly improve the coupling ability with Zn^{2+} ions.

Ex-situ XRD patterns show that a new characteristic peak attributed to $Zn(CF_3SO_3)_2[Zn(OH)_2]_3\cdot xH_2O$ was observed when the discharge voltage was varied from 1.8 V to 0 V and disappeared again during re-charging (Fig. 3f) [69,70]. A clear formation of flaky zinc salts was also observed at state C by SEM image, and EDS-mapping shows the distribution of S and Zn elements (Fig. S14 in Supporting information). The formation of zinc salts is attributed to the aggregated adsorption of Zn^{2+} ions on the CSs-800 cathode during the discharge process and the interaction with $CF_3SO_3^-$ and OH^- ions in the electrolyte. Considering that protons are produced by the consumption of OH^- ions in H_2O, they may be involved in electrochemical storage. To verify this idea, electrochemical tests were performed using HCF_3SO_3 electrolytes with different pH. As the proton content in the electrolyte increases, the capacity of CSs-800 is elevated, verifying the auxiliary role of protons in the storage process (Fig. S15a in Supporting information) [71]. And when using a proton-free electrolyte ($Zn(CF_3SO_3)_2$/ACN), the CSs-800 based ZIHCs also shows less than its specific capacity in $Zn(CF_3SO_3)_2/H_2O$ (Fig. S15b in Supporting information).

The effects of carbonyl and pyridine-N functional groups with electrochemical redox-active activity on the cathode storage performance of CSs-800 were investigated by density functional theory (DFT) calculations [72]. Reduced density gradient (RDG) plots based on the reaction between pyridine-N and Zn^{2+} ion model show that the green spike is observed in the horizontal coordinate region in the range of −0.01 ∼ −0.02 a.u., which suggests that the pyridine site can interact with Zn^{2+} ions (Fig. 4a) [73]. Meanwhile, RDG plot of the carbonyl and Zn^{2+} ion model also shows green spikes representing the interaction of carbonyl and Zn^{2+} ion in the range of −0.01 ∼ −0.022 a.u. for the horizontal coordinate region (Fig. 4b). Moreover, the interaction of carbonyl group with Zn^{2+} ion is significantly greater than the interaction of pyridine-N with Zn^{2+} ion, which suggests that carbonyl group is more strongly cou-

pled with Zn^{2+} ion. When the carbonyl and pyridine-N functional groups were paired with each other in the model (Fig. 4c), they demonstrated a more robust chelation of Zn^{2+} ion, which is also shown in the RDG plots (Fig. 4d). Specifically, the relative adsorption energies (ΔE_a) of CSs cathode modified with different functional groups for Zn^{2+} ion were calculated in detail. Smaller values of ΔE_a were associated with higher electrophilic properties and reactivity of the functional motifs towards the Zn^{2+} ion. The carbon superstructure modifies with both carbonyl and pyridine-N active sites with an ΔE_a of 2.38 eV, which is greater than that of the ΔE_a with a single pyridine-N (0.68 eV) and a single carbonyl group (1 eV) (Fig. 4e). Similarly, $CF_3SO_3^-$ electrosorption based on the synergistic interactions of carbonyl and pyridine-N motifs in carbon cathode also shows more favorable conformation compared to carbon cathode with a single active center (Fig. S16 in Supporting information).

Differential charge density isosurface simulations of the adsorption interface based on the optimized model were carried out to study in depth the charge transfer and bonding of heteroatoms during storage. The yellow region represents the electron-enriched region and the blue represents the electron-deficient region, from which it can be seen that the electrons are transferred from the vicinity of zinc to the region where the pyridine-N and carbonyl groups are located, revealing the interactions of the electroactive carbonyl and pyridine-N group order on zinc [74]. In addition, the simulation results show that the modification of the heteroatoms effectively reduces the energy barrier of the interaction of zinc ions with the carbon cathode. The analysis in the Bader charge diagram yields 0.66 e charge transfer from the yellow region to the blue region (Fig. 4f), implying that the effective access of zinc ions from the electrochemically active carbonyl and pyridine-N functional group strengthens the charge storage capacity of the carbon cathode. Theoretical calculations further demonstrated that heteroatom modification could make carbon cathode more efficient for charge storage and accelerate the ion transfer rate.

In summary, a three-dimensional carbon superstructure with a definite structure is constructed by the solvothermal method. In particular, tetrachloro-*p*-benzoquinone (TBQ) and 2,6-diaminoanthraquinone (DAQ) were prepared under the condition of the coupling reaction without a noble metal catalyst, and the organic motifs were induced to construct the spherical nano-flower-like carbon superstructure. ZIHCs based on CSs-800 can provide an ultra-high energy density of 152 Wh/kg and ultra-stable cycle life, with 92.7% capacity retained after 300,000 cycles at 20 A/g. The excellent electrochemical performance was attributed to the obtained three-dimensional carbon superstructure. This kind of superstructure can effectively prevent the self-stacking of carbon structure, shorten the ion diffusion distance and ensure the high density of the active center. This also facilitates the alternating binding of $Zn^{2+}/CF_3SO_3^-$ ions at the carbon-active site and imparts incredible structural stability to the carbon material. This paper describes the synthesis of an advanced porous carbon cathode material, and the basic understanding of its charge storage mechanism is presented.

Declaration of competing interest

The authors declare that they have no known competing financial interests or personal relationships that could have appeared to influence the work reported in this paper.

CRediT authorship contribution statement

Chengmin Hu: Writing – original draft, Software, Resources, Methodology, Formal analysis. **Pingxuan Liu:** Project administration, Methodology, Investigation. **Ziyang Song:** Writing – original draft, Software, Resources, Methodology, Funding acquisition. **Yaokang Lv:** Methodology, Funding acquisition. **Hui Duan:** Supervision, Project administration, Investigation. **Li Xie:** Validation, Supervision, Resources. **Ling Miao:** Writing – review & editing, Supervision, Resources, Funding acquisition. **Mingxian Liu:** Writing – review & editing, Supervision, Resources, Project administration, Funding acquisition. **Lihua Gan:** Writing – review & editing, Software, Methodology, Funding acquisition.

Acknowledgments

This work is financially supported by the National Natural Science Foundation of China (Nos. 22272118, 22172111, 21905207, and 22309134), the Science and Technology Commission of Shanghai Municipality (Nos. 22ZR1464100, 20ZR1460300, and 19DZ2271500), China Postdoctoral Science Foundation (No. 2022M712402), Shanghai Rising-Star Program (No. 23YF1449200), Zhejiang Provincial Science and Technology Project (No. 2022C01182), and the Fundamental Research Funds for the Central Universities (Nos. 22120210529 and 2023–3-YB-07).

Supplementary materials

Supplementary material associated with this article can be found, in the online version, at doi:10.1016/j.cclet.2024.110381.

References

[1] L. Dong, W. Yang, W. Yang, et al., J. Mater. Chem. A 7 (2019) 13810–13832.
[2] H. Tang, J. Yao, Y. Zhu, Adv. Energy Mater. 11 (2021) 2003994.
[3] Y. Wang, S. Sun, X. Wu, et al., Nano-Micro Lett. 15 (2023) 78.
[4] X. Zhang, Z. Pei, C. Wang, et al., Small 15 (2019) 1903817.
[5] X. Zhang, X. Wu, X. Wang, et al., J. Energy Storage 72 (2023) 108798.
[6] Z. Song, L. Miao, H. Duan, et al., Angew. Chem. Int. Ed. 63 (2024) e202401049.
[7] Y. Zhang, Z. Song, L. Miao, et al., Adv. Funct. Mater. 34 (2024) 2405710.
[8] T. Shi, C. Hu, Q. Huang, et al., Chem. Eng. J. 500 (2024) 157627.
[9] X. Xu, Y. Chen, W. Li, et al., Small 19 (2023) 2207517.
[10] J. Feng, D. Zheng, R. Yin, et al., Small Struct. 4 (2023) 2200340.
[11] X. Pan, Q. Li, T. Wang, et al., Nanoscale 16 (2024) 3701–3713.
[12] H. Zhang, Q. Liu, Y. Fang, et al., Adv. Mater. 31 (2019) 1904948.
[13] P. Zhang, Y. Li, G. Wang, et al., Adv. Mater. 31 (2019) 1806005.
[14] Z. Guo, Y. Ma, X. Dong, et al., Angew. Chem. Int. Ed. 57 (2018) 11737–11741.
[15] F. Zeng, X. Gong, Z. Xu, et al., J. Mater. Chem. A 11 (2023) 26698–26706.
[16] C. Leng, Z. Zhao, J. Guo, et al., Chem. Commun. 57 (2021) 8778–8781.
[17] Z. Li, J. Tan, Y. Wang, et al., Energy Environ. Sci. 16 (2023) 2398–2431.
[18] H. Liu, D. Tong, L. Peng, et al., ACS Appl. Energy Mater. 6 (2023) 6752–6759.
[19] S. Gourley, R. Brown, B. Adams, et al., Joule 7 (2023) 1415–1436.
[20] Y. Zhao, C. Yang, Y. Yu, Chin. Chem. Lett. 35 (2024) 108865.
[21] Z. Sun, S. Chu, X. Jiao, et al., J. Energy Storage 75 (2024) 109571.
[22] F. Wei, Y. Zeng, Y. Guo, et al., Chem. Eng. J. 468 (2023) 143576.
[23] L. Zhao, W. Jian, J. Zhu, et al., ACS Appl. Mater. Interfaces 14 (2022) 43431–43441.
[24] H. Heo, K. Yun, G.H. An, J. Alloys Compd. 965 (2023) 171229.
[25] J. Yao, F. Li, R. Zhou, et al., Chin. Chem. Lett. 35 (2024) 108354.
[26] Y. Wang, J. Cao, J. Guo, et al., J. Alloys Compd. 915 (2022) 165418.
[27] H. Xu, W. He, Z. Li, et al., Adv. Funct. Mater. 32 (2022) 2111131.
[28] W. Zhang, H. Kang, Z. Gu, et al., J. Energy Storage 61 (2023) 106715.
[29] L.Y. Gao, X.W. Zhong, Z.T. Li, et al., Chem. Commun. 60 (2024) 1269–1272.
[30] C. Nason, A. Saroja, Y. Lu, et al., Nano-Micro Lett. 16 (2024) 1.
[31] Q. Huang, L. Huang, Y. Jin, et al., Chem. Eng. J. 482 (2024) 148912.
[32] H. Li, Q. Liao, Y. Liu, et al., Small 20 (2023) 2307184.
[33] Y. Liu, L. Wu, Nano Energy 109 (2023) 108290.
[34] Z. Li, D. Chen, Y. An, et al., Energy Storage Mater. 28 (2020) 307–314.
[35] H. Li, J. Wu, L. Wang, et al., Chem. Eng. J. 428 (2022) 131071.
[36] Q. Wang, Y. Chen, X. Jiang, et al., Energy Storage Mater. 48 (2022) 164–171.
[37] X. Cao, Z. Yin, H. Zhang, Energy Environ. Sci. 7 (2014) 1850–1865.
[38] H. Sun, C. Liu, D. Guo, et al., RSC Adv. 12 (2022) 24724–24733.
[39] L. Yang, X. He, Y. Wei, et al., J. Power Sources 542 (2022) 231743.
[40] C. Zhu, R. Long, L. Zhu, et al., J. Colloid Interface Sci. 652 (2023) 590–598.
[41] M. Mansuer, L. Miao, Y. Qin, et al., Chin. Chem. Lett. 34 (2023) 107304.
[42] X. Yang, C. Hu, Y. Chen, et al., J. Energy Storage 104 (2024) 114509.
[43] W. Jian, W. Zhang, X. Wei, et al., Adv. Funct. Mater. 32 (2022) 2209914.
[44] F. Wu, F. Du, P. Ruan, et al., J. Mater. Chem. A 11 (2023) 11254–11263.
[45] L. Hu, L. Bo, N. Wang, et al., Chem. Eng. J. 479 (2024) 147570.
[46] F. Mo, Y. Wang, T. Song, et al., J. Energy Storage 72 (2023) 108228.
[47] Y. Shao, Z. Sun, Z. Tian, et al., Adv. Funct. Mater. 31 (2020) 2007843.
[48] N. Li, X. Zhang, S. Zhao, et al., Chin. Chem. Lett. 34 (2023) 107669.

[49] X. Gao, H. Deng, Y. Fang, et al., Chin. Chem. Lett. 34 (2023) 107919.
[50] J. Huang, C. Liu, Y. Jin, et al., Chem. Eng. J. 461 (2023) 141930.
[51] L. Wang, M. Peng, J. Chen, et al., ACS Nano 16 (2022) 2877–2888.
[52] B. Chen, N. Huang, Z. Zhai, et al., Small 20 (2024) 2310523.
[53] W. Li, Y. Wang, B. Wang, et al., Angew. Chem. Int. Ed. 63 (2024) e202308951.
[54] Z. Xu, M. Li, W. Sun, et al., Adv. Mater. 34 (2022) 2200077.
[55] D. Zhang, L. Miao, Z. Song, et al., Energy Fuels 38 (2024) 12510–12527.
[56] A. Awati, R. Yang, T. Shi, et al., Angew. Chem. Int. Ed. 63 (2024) e202407491.
[57] X. Wang, K. Zou, W. Wu, et al., Chin. Chem. Lett. 33 (2022) 3883–3888.
[58] W. Li, H. Xu, H. Zhang, et al., Nat. Commun. 14 (2023) 5235.
[59] Q. Sun, T. Sun, J. Du, et al., Angew. Chem. Int. Ed. 62 (2023) e202307365.
[60] Z. Tie, Y. Zhang, J. Zhu, et al., J. Am. Chem. Soc. 144 (2022) 10301–10308.
[61] C. Hou, Y. Wang, L. Zou, et al., Adv. Mater. 33 (2021) 2101698.
[62] Y. Dai, X. Liao, R. Yu, et al., Adv. Mater. 33 (2021) 2100359.
[63] S. Wu, Y. Chen, T. Jiao, et al., Adv. Energy Mater. 9 (2019) 1902915.
[64] L. Dong, X. Ma, Y. Li, et al., Energy Storage Mater. 13 (2018) 96–102.
[65] X. Zheng, Z. Song, D. Zhang, J. Mater. Chem. A 12 (2024) 15352–15360.
[66] Q. Huang, Y. Jin, L. Huang, et al., J. Mater. Chem. A 11 (2023) 12297–12307.
[67] Y. Zhang, Z. Song, L. Miao, et al., Angew. Chem. Int. Ed. 63 (2024) e202316835.
[68] F. Xie, H. Li, X. Wang, et al., Adv. Energy Mater. 11 (2021) 2003419.
[69] S. Zheng, D. Shi, D. Yan, et al., Angew. Chem. Int. Ed. 61 (2022) e202117511.
[70] C. Hu, Y. Chen, Z. Song, et al., J. Mater. Chem. A 12 (2024) 12818–12825.
[71] C. Hu, X. Yang, P. Liu, et al., J. Mater. Chem. A 12 (2024) 11867–11874.
[72] F. Lu, J. Comput. Chem. 33 (2012) 580–592.
[73] K. Zou, H. Tan, L. Wang, et al., J. Colloid Interface Sci. 537 (2019) 475–485.
[74] C. Li, Z. Sun, T. Yang, et al., Adv. Mater. 32 (2020) 2003425.